

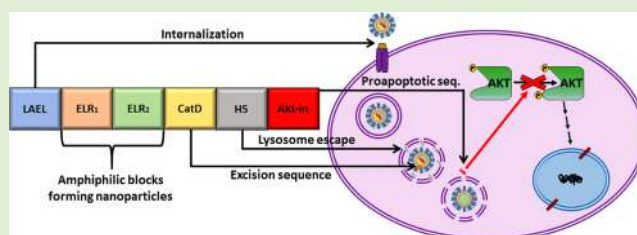
# Self-Assembling ELR-Based Nanoparticles as Smart Drug-Delivery Systems Modulating Cellular Growth via Akt

Juan Gonzalez-Valdivieso,<sup>1</sup> Alessandra Girotti, Raquel Muñoz, J. Carlos Rodriguez-Cabello,<sup>1</sup> and F. Javier Arias<sup>1\*</sup>

BIOFORGE (Group for Advanced Materials and Nanobiotechnology), CIBER-BBN, University of Valladolid, 47011 Valladolid, Spain

**S** Supporting Information

**ABSTRACT:** This work investigates the physicochemical properties and in vitro accuracy of a genetically engineered drug-delivery system based on elastin-like block recombinamers. The DNA recombinant techniques allowed us to create this smart complex polymer containing bioactive sequences for internalization, lysosome activation under acidic pH, and blockage of cellular growth by a small peptide inhibitor. The recombinant polymer reversibly self-assembled when the temperature was increased above 15 °C into nanoparticles with a diameter of 72 nm and negative surface charge. Furthermore, smart nanoparticles were shown to enter in the cells via clathrin-dependent endocytosis and properly blocked phosphorylation and consequent activation of Akt kinase. This system provoked apoptosis-mediated cell death in breast and colorectal cancer cells, which possess higher expression levels of Akt, whereas noncancerous cells, such as endothelial cells, fibroblasts, and mesenchymal stem cells, were not affected. Hence, we conclude that the conformational complexity of this smart elastin-like recombinamer leads to achieving successful drug delivery in targeted cells and could be a promising approach as nanocarriers with bioactive peptides to modulate multiple cellular processes involved in different diseases.



## 1. INTRODUCTION

One of the limitations of modern medicine is the lack of efficient drug carriers. Such carriers should accomplish their main function, namely, release of a drug in a targeted tissue, so as to achieve two benefits: an increase in drug efficacy and a reduction in possible adverse side effects.<sup>1</sup> The development of a good carrier for a specific drug is of particular importance as, in some cases, the therapeutic dose of a drug is so high that it cannot be used without causing severe damage to other organs.<sup>2</sup> One of the most recent therapeutic approaches is based on smart advanced biomaterials<sup>3,4</sup> as they are able to overcome the limitations and improve the action of therapeutic agents.<sup>5,6</sup> Multifunctional carriers have been proposed to overcome these deficiencies.<sup>7</sup> Although significant progress has been made in the field of synthetic devices with improved polymerization efficiency and lower polydispersities, genetically engineered polymers provide us the control to build advanced delivery carriers with acquired functionalities.<sup>8</sup>

Elastin-like recombinamer (ELR) is one such biomaterial. ELRs are biopolymers based on short pentapeptide repeats found in the sequence of natural elastin, mainly the VPGXG pentapeptide, where X can be any amino acid except proline. The term ELR refers to those elastin-like polypeptides manufactured using genetic-engineering techniques. Recombinant DNA technology allows us to design ELRs with full control over the amino acid sequence and includes different functionalities and bioactive sequences.<sup>9,10</sup> As such, ELRs

presenting characteristic features are a novel alternative for the development of new biomedical devices because of their biological and mechanical properties, such as biocompatibility, biodegradability, and thermally and environmentally responsive behavior.<sup>11</sup> Moreover, ELRs have gained notable interest in the last few years due to their lack of toxicity and immunogenicity as a consequence of their protein nature. ELRs exhibit an inverse temperature transition, which means that below a characteristic temperature, the so-called transition temperature ( $T_t$ ), they remain soluble in a random coil conformation, self-assembling hydrophobically above this  $T_t$  and resulting in the reversible formation of coacervates due to a conformational reorganization at the molecular level. Coacervation of the polymer backbone can be triggered by different factors, including temperature, pH, light, ion concentration, etc. In addition, their stimulus-responsive behavior can be tuned as  $T_t$  is controlled by the amino acid composition of the recombinamer.<sup>12</sup> Given their cell-friendly behavior, tunable mechanical properties, thermal sensitivity, and ability to self-assemble, they are useful biomaterials for most applications in the fields of nanotechnology and biomedicine and, specifically, for controlled drug delivery.<sup>13–17</sup>

**Received:** February 11, 2019

**Revised:** April 2, 2019

**Published:** April 4, 2019

Advanced drug-delivery systems enable one to control the release of drugs in a specific cell or tissue, so smart bioresponsive biomaterials that can self-assemble and act under certain stimuli emerge as promising approaches for the achievement of reduced doses of the drugs and limited side effects.

Due to the poor tumor accumulation of standard drugs used in chemotherapy, carriers have become an interesting approach for drug-delivery purposes.<sup>18</sup> Nanoparticle (NP)-based delivery can reduce side effects by redistributing drug accumulation away from critical organs, such as the kidney or liver, thus allowing the administration of larger doses than is possible with free drugs.<sup>19</sup> As tumors have an aberrant vascular endothelium and enhanced vascular permeability, 10–100 nm-sized nanoparticles accumulate in tumors because of the enhanced permeability and retention (EPR) effect.<sup>20</sup> This effect arises due to the fact that tumors have no functional lymphatic vessels, thus resulting in inefficient drainage from the tumor tissue.<sup>21,22</sup> As such, nanoparticles are able to enter the interstitial space but are not efficiently removed,<sup>23</sup> thus being retained in the tumor tissue.

The choice of the specific target in drug delivery makes the difference between whether healthy tissues are affected or not.<sup>24</sup> Cancer is one of the potential applications of drug-delivery systems as it is one of the most common diseases worldwide. In this regard, cancer markers, such as overexpressed receptors and cytoplasmic proteins, are the most widely used targeting systems due to their higher expression in cancerous cells when compared to noncancerous cells.<sup>21,25</sup> Consequently, novel strategies that target overexpressed proteins could be of interest when determining how to stop uncontrolled cell proliferation, which is markedly faster in cancerous cells. Of these proteins, Akt stands out due to its important role in controlling multiple signaling pathways and processes in cells.<sup>26</sup> Akt is a protein kinase that plays a central role in the regulation of multiple cellular processes, enhancing cellular proliferation, metabolism, and motility and inhibiting apoptosis.<sup>26</sup> It has three differentiated functional regions, namely, the N-terminal pleckstrin homology domain (PH), the central catalytic domain, and, finally, the C-terminal hydrophobic region.<sup>27</sup> In response to growth factors, Akt is activated by products of phosphatidylinositol triphosphate generated by PI3K. These lipid products bind to the PH domain of Akt, thereby inducing a conformational change and allowing PDK1 to phosphorylate threonine 308. Phosphorylation of serine 473 and membrane anchoring are also required after threonine 308 phosphorylation for final activation of Akt kinase.<sup>28</sup> There are three different isoforms (Akt1, Akt2, and Akt3) in mammalian cells. Akt1 is the most abundant isoform and is overexpressed in multiple types of cancers, such as colon, pancreatic, breast, ovarian, and lung neoplastic diseases.<sup>29</sup> In light of this, Hiromura et al. have developed a small peptide (Akt-in) that accurately prevents phosphatidylinositol species from binding to the pleckstrin homology domain (PH) of Akt by causing conformational changes, thereby inhibiting membrane translocation and Akt activation. This inhibitor prevents Akt kinase activity and, consequently, a biological response downstream. Moreover, Akt-in inhibits both *in vitro* proliferation and antiapoptosis action as well as *in vivo* tumor progression.<sup>30</sup>

The objectives of this study were to synthesize and characterize a smart stimulus-responsive therapeutic system that can be modulated for application in different cells. Only recombinant technology allows us to create multifunctional

block copolymers that can self-assemble into versatile nanoparticles (NPs) carrying the peptidic inhibitor of Akt, in a targeted and protected manner, and are specifically released in the intracellular environment. In light of the above, we have developed ELR nanoparticles carrying the peptidic inhibitor of protein kinase Akt (Akt-in). Moreover, we have determined *in vitro* the therapeutic window in which tumor cells are affected and normal ones not and have studied their internalization pathway and intracellular trafficking.

## 2. MATERIALS AND METHODS

**2.1. Chemical Reagents and Cell Lines.** Genes for LAEL, cathepsin D (CatD)-sensitive peptide, H5 peptide, and Akt-in were acquired from NZYTECH (Portugal). *Escherichia coli* BLR (DE3) strain was supplied by Novagen. Chloroquine, filipin, amiloride, and monodansylcadaverine were purchased from Sigma-Aldrich. Pepstatin A was acquired from Apollo Scientific. Primary antibodies against Akt (#9272),  $\rho$ -Akt Ser473 (#9271), and glyceraldehyde 3-phosphate dehydrogenase (GAPDH) (sc-32233) were purchased from Cell Signaling and Santa Cruz Biotechnology. Goat secondary antibodies against rabbit (ab6721) and mouse (ab205719) were supplied by Abcam. Cell lysis buffer and Bradford reagent were supplied by Sigma-Aldrich. Human adipose-derived mesenchymal stem cells (hMSCs, R7788-115), basal medium Dulbecco's modified Eagle's medium (DMEM), minimum essential medium (MEM), fetal bovine serum (FBS), penicillin streptomycin solution, trypsin–ethylenediaminetetraacetic acid (EDTA), Dulbecco's phosphate buffered saline (DPBS), glutamine, nonessential amino acids (NEAA), and the LIVE/DEAD viability/cytotoxicity kit for mammalian cells were supplied by Invitrogen. Human umbilical vein endothelial cells (HUVEC cc-2517), medium 200, low serum growth supplement (LSGS), L-15 medium, and gentamicin/amphotericin solution were purchased from Gibco. Human foreskin fibroblasts (HFF-1, SCRC-1041) were purchased from the American Type Culture Collection (ATCC). Human breast cancer (MCF-7, 86012803 ECACC) and human colorectal cancer (Caco-2, 86010202 ECACC) cell lines were supplied by Sigma-Aldrich.

**2.2. ELR Design, Bioproduction, and Purification.** The elastin-like recombinamers (ELRs) used in this work were obtained as described elsewhere.<sup>31</sup> The final fusion genes with a fully controlled composition and chain length were constructed by sequential introduction of the monomer gene segments in a stepwise manner using the recursive directional ligation method. The DNA sequence of every cloning step was corroborated by DNA sequencing. Expression vectors containing the selected ELR genes were transformed into *E. coli* BLR (DE3) strain (Novagen) for production. The ELR was then bioproduced in *E. coli* in a 15 L bioreactor (Applikon Biotechnology, The Netherlands) and purified by several cooling and heating purification cycles (inverse transition cycling) following centrifugation, taking advantage of the ability of these recombinamers to aggregate above their transition temperature. Endotoxins were removed from the ELR by way of additional NaCl and NaOH treatments.<sup>32</sup> Finally, the polymer was dialyzed against ultrapure water type I, sterilized by filtration (0.22  $\mu$ m filters Nalgene), and freeze-dried prior to storage. The molecular weight and purity of the recombinamers were determined by sodium dodecyl sulfate polyacrylamide gel electrophoresis (SDS-PAGE) and matrix-assisted laser desorption/ionization time-of-flight mass spectrometry (MALDI-TOF/MS), respectively. The amino acid composition was further verified by high-performance liquid chromatography (HPLC) and NMR spectroscopy by the Instrumental Techniques Laboratory of the University of Valladolid. Endotoxin levels were measured using the Endosafe-PTSTM test (Charles River).

**2.3. Differential Scanning Calorimetry (DSC).** DSC experiments were performed using a Mettler Toledo 822e with a liquid-nitrogen cooler. Both temperature and enthalpy were calibrated against an indium standard. Solutions were prepared by dissolving the ELRs in PBS (pH 7.4) at 50 mg/mL. A 20  $\mu$ L aliquot of each solution

and its corresponding PBS reference were subjected to an initial isothermal stage (5 min at 0 °C to stabilize the temperature and state of the samples), followed by heating from 0 to 60 °C at 5 °C/min. The enthalpy values for endothermic processes were taken as negative and exothermic values as positive.

**2.4. Particle Size and  $\zeta$ -Potential.** The particle size and  $\zeta$ -potential of the polymers were determined by dynamic light scattering (DLS) using a Zetasizer Nano ZS (Malvern Instruments Ltd., U.K.) at a temperature of 37 °C. Solutions of both ELRs were prepared by dissolving the ELRs in PBS (pH 7.4) or ultrapure water type I (pH 7.4) when indicated. The solutions were stored at 4 °C overnight to allow complete dissolution of the recombinamers and filtered using a 0.45  $\mu$ m poly(vinylidene difluoride) (PVDF) syringe filter. The samples were then incubated for 30 min at 37 °C to allow supramolecular assembly to occur and then introduced into polystyrene cuvettes and stabilized for 2 min at the desired temperature. For bovine serum albumin (BSA) interaction experiments, ELRs were incubated in 5% BSA PBS for 1, 2, or 3 h at 37 °C after overnight dissolution and then filtered, introduced into polystyrene cuvettes, and stabilized for 2 min at the desired temperature. Autocorrelation functions were used to obtain the size distribution and polydispersity index (PDI). Z-average mean (nm) and  $\zeta$ -potential (mV) were used for data analysis. Three different samples were analyzed.

**2.5. Transmission Electron Microscopy (TEM).** Solutions were prepared by dissolving the ELRs in ultrapure water type I and kept at 4 °C overnight to allow complete dissolution of the polymers. The sample was incubated for 30 min at 37 °C to allow supramolecular assembly to occur and stained with uranyl acetate solution (1.0 wt %) to enhance the contrast of the nanoparticles on a carbon-coated copper grid, followed by solvent evaporation. Samples were observed using a JEM-2200 electron microscope operating at 200 kV.

**2.6. Surface Tension by the Pendant Drop Technique.** The critical micellar concentration (CMC) of the different ELR solutions in both PBS and ultrapure water type I was determined from surface tension measurements derived from a drop-shape analysis using the pendant drop technique.<sup>33</sup> The changes in the shape of the resulting drop at the air/water interface upon increasing the ELR concentration previously stabilized at 37 °C for 15 min from a blank solution to 20  $\mu$ m were monitored using SCA 20 software of a Data Physics OCA20 instrument, which scaled the profile of the drop hanging from a straight precision dosing needle. The drops (4  $\mu$ L at 0.5  $\mu$ L/s) were infused using a 500  $\mu$ L Gastight Hamilton syringe. Three drops were analyzed per condition, and the CMC was determined from the point of slope change after plotting the change in surface tension values versus log(concentration) of the ELRs.

**2.7. Cell Culture.** MCF-7 and Caco-2 cells were maintained in MEM supplemented with 10% FBS, 2 mM glutamine, 1% NEAA, 100 U/mL penicillin, and 0.1 mg/mL streptomycin at 5% CO<sub>2</sub> and 37 °C. MDA-MB-231 cells were cultured in L-15 medium supplemented with 10% FBS, 100 U/mL penicillin, and 0.1 mg/mL streptomycin at 0% CO<sub>2</sub> and 37 °C. hMSC and HFF-1 cells were cultured in DMEM supplemented with 100 U/mL penicillin, 0.1 mg/mL streptomycin, and 10 and 15% FBS at 10% CO<sub>2</sub> and 37 °C, respectively. HUVEC cells were grown in Medium 200 supplemented with 1% gentamicin/amphotericin and LSGS at 5% CO<sub>2</sub> and 37 °C. When required, cells were detached using a solution of 0.05% trypsin-EDTA. Cells were seeded onto 96-well plates at a quantity of  $2 \times 10^4$  cells per cm<sup>2</sup> for tumor cells and  $1 \times 10^4$  cells per cm<sup>2</sup> for primary cells to maintain the same levels of confluence for all the cell lines overnight prior to the treatment.

**2.8. Confocal Microscopy.** MDA-MB-231 cells were treated with fluorescein-conjugated ELRs at 0.5 mg/mL for 90 min. Confocal images were taken using a Leica TCS SPS confocal microscope. Cellular nuclei were stained with 4',6-diamidino-2-phenylindole (DAPI).

**2.9. Flow Cytometry.** MDA-MB-231 cells ( $5 \times 10^5$  cells in 6-well plates) were incubated with complete medium containing fluorescein-labeled nanoparticles at 0.5 mg/mL for 90 min. Cells were washed with PBS, trypsinized, and centrifuged for 10 s at 13200 rpm. The

supernatant was discarded, and the pellet was resuspended in PBS. Flow cytometry analysis was performed to assess the fluorescein internalized in cells (Gallios flow cytometer, Beckman Coulter).

**2.10. Cell Viability.** MCF-7, MDA-MB-231, Caco-2, hMSC, HFF-1, and HUVEC were treated with ELRs at three different concentrations (0.25, 0.5, and 1 mg/mL) for different times (30, 60, 90, and 120 min). Live and dead staining (LIVE/DEAD viability/cytotoxicity assay kit, Invitrogen) was used according to the manufacturer's instructions. Briefly, a stock solution of the LIVE/DEAD reagents (1  $\mu$ m of calcein AM and 2  $\mu$ m of EthD-1 in 10 mL of DPBS) was prepared, samples (100  $\mu$ L) were distributed in each well and incubated for 20 min in the dark, and then the fluorescence intensity emission was measured at 525 and 645 nm after excitation at 485 and 525 nm (SpectraMax M5e Molecular Devices microplate reader). Additionally, photographic images of cultures were taken using a Nikon eclipse Ti-SR (Japan) fluorescence microscope. Three independent experiments, each in triplicate, were performed.

**2.11. Cell Proliferation.** HFF-1, hMSC, and HUVEC cells were seeded in 96-well plates. After 24 h incubation, cells were treated with ELRs at two different concentrations (1 and 0.5 mg/mL) for 72 h. Confluence percentages were determined each 4 h by Cytosmart OMNI software (Cytosmart, The Netherlands). Two independent experiments, each in quadruplicate, were performed.

**2.12. Western Blot.** Caco-2 and MDA-MB-231 cells were incubated with complete medium containing nanoparticles at 0.5 mg/mL for 2 h. Cells were lysed and protein concentrations measured using Bradford's reagent. Thus, 50  $\mu$ g of protein was separated using standard SDS-PAGE and transferred to PVDF membranes. Blocking was performed with 5% defatted dry milk in PBS (pH 7.4) for 1 h at room temperature. Primary Akt,  $\rho$ -Akt, and glyceraldehyde 3-phosphate dehydrogenase (GAPDH) antibodies were used in PBS with 0.5% defatted dry milk and 0.1% Tween-20 at 1:1000 and 1:2000, respectively, according to the manufacturer's instructions. After extensive washing, secondary HRP-linked antibodies were used at a 1:10 000 dilution. Specific proteins were visualized using the enhanced chemoluminescent substrate.

**2.13. Apoptosis/Necrosis Assay.** Caco-2 and MDA-MB-231 cells were incubated with a complete medium containing nanoparticles at 0.5 mg/mL for 2 h. Fluorescein isothiocyanate (FITC)-conjugated annexin V and propidium iodide staining (Annexin V FITC Assay Kit, Cayman Chemical) was used according to the manufacturer's instructions, and the fluorescence intensity emission was measured (SpectraMax M5e Molecular Devices microplate reader) at 535 and 595 nm after excitation at 488 and 560 nm, respectively. Three independent experiments, each in triplicate, were performed.

**2.14. Assessment of the Internalization Pathway.** Caco-2 and MDA-MB-231 cells were pretreated with 25  $\mu$ m of chloroquine, 1  $\mu$ g/mL filipin, 5  $\mu$ g/mL amiloride, and 100  $\mu$ m of monodansylcadaverine in minimal medium for 30 min. After treatment with the inhibitor, the medium was replaced with a fresh one containing 0.5 mg/mL polymer for 2 h. Finally, the cell viability assay was carried out as described above. Three independent experiments, each in triplicate, were performed.

**2.15. Assessment of Intracellular Trafficking.** Caco-2 and MDA-MB-231 cells were preincubated with 100  $\mu$ m of Pepstatin A at 37 °C in each cell culture in complete medium for 16 h. After Pepstatin A treatment, the medium was replaced with a fresh one containing 0.5 mg/mL polymer for 2 h. The cell viability was then determined as described above. Three independent experiments, each in triplicate, were performed.

**2.16. Statistical Analysis.** Data are reported as mean  $\pm$  standard deviation (SD) ( $n = 3$ ). Statistical analysis involved a variance analysis in combination with a subsequent analysis using the Bonferroni method. A  $p$  value of less than 0.05 was considered to be statistically significant. \* $p < 0.05$ , \*\* $p < 0.01$ , \*\*\* $p < 0.001$ . Data were handled using SPSS Statistics software version 20 (IBM).

### 3. RESULTS AND DISCUSSION

**3.1. ELR Design.** ELRs are able to self-assemble into different structures depending on their composition, with amphiphilic ELR-based diblocks forming vesicles or micelles above their transition temperature.<sup>34</sup> The genetic design of ELRs allows us to control their characteristic  $T_t$  below the physiological temperature of 37 °C, thus resulting in coacervate formation. One disadvantage of therapeutic molecules, such as drugs or peptides, is their short circulating half-lives, thus meaning that frequent administration of high concentrations is required to obtain the therapeutic level.<sup>35</sup> Therapeutic agents have to pass through several biological barriers to reach the tumor tissue and ensure an effective dose. Furthermore, systemic administration results in high toxicity, especially for healthy tissues.<sup>36,37</sup> ELR-based carriers play an interesting role regarding overcoming all these limitations as they are able to extend the circulating half-life of therapeutic peptides or drugs and also improve their targeting and pharmacokinetics.

We designed two different polymers, control and Akt-in, both based on an amphiphilic backbone consisting of a hydrophilic block formed by glutamic acid and a hydrophobic block formed by isoleucine. The glutamic acid block is based on the monomer [(VPGVG)<sub>2</sub>-(VPGEG)-(VPGVG)<sub>2</sub>]<sub>10</sub>, whereas the isoleucine block is based on [VGIPG]<sub>60</sub>. This amphiphilic ELR construct has been shown to self-assemble into highly monodisperse and stable nanoparticles with a size of 55 nm.<sup>34</sup> We also included a small sequence containing three lysine residues, to which different molecules can be attached by covalent binding, at the amino terminus. According to the literature, we expected that our polymers would enter the cell via endosomes and continue to lysosomes;<sup>38</sup> therefore, we included an LAEL sequence, a small peptide that undergoes a structural change from random coil to  $\alpha$ -helix after acidification of the pH in the endosome/lysosome (pH 5) and triggers destabilization and permeabilization of the vesicle membrane, thereby allowing endosomal escape, in both polymers.<sup>39</sup> The control ELR construct was designed with an amphiphilic backbone containing the three lysine residues and the LAEL sequence. This construct was used to clarify any effect of the ELR modules. Moreover, the LAEL sequence was included in the control polymer to study possible cytotoxicity due to internalization of the nanoparticles and their escape from endosomes/lysosomes. Furthermore, we added different bioactive blocks to the functional polymer. For example, cathepsin D (CatD) is a lysosomal aspartyl endopeptidase<sup>40</sup> that is overexpressed in cancer cells compared to normal cells and is thought to promote tumor invasion and growth. As such, we included a cathepsin D-sensitive sequence to allow its enzymatic action and the Akt inhibitor to reach the cytoplasm. To allow the Akt inhibitor to escape from the endosome/lysosome, we added the H5 codifying sequence, a histidine-rich peptide that undergoes a conformational change from a  $\beta$ -structure to a disordered structure at acidic pH<sup>41</sup> as a result of protonation of the imidazole ring in histidine and provides lysosomal membrane permeation. Finally, we included the sequence codifying the peptide Akt-in, a small peptide of fifteen amino acids, which acts as an inhibitor of protein kinase Akt. Indeed, this inhibitor prevents Ser473-phosphorylation, which is a key step, upon binding to Akt protein<sup>30</sup> before being active in the cellular cytoplasm and playing a key role in multiple signaling pathways.<sup>28</sup> In light of

the above, our hypothesis for the mechanism of action is that once CatD has digested the cathepsin D-sensitive sequence, the H5 peptide and inhibitor will be released into the cellular cytoplasm and will be able to bind to Akt protein and block it.

The amino acid sequences for the different ELR constructs (control and Akt-in, respectively) are (1) MGKKKPV-LAELLAELLAEL[(VPGVG)<sub>2</sub>-(VPGEG)<sub>10</sub>-(VPGVG)<sub>2</sub>]-[VGIPG]<sub>60</sub>-V and (2) MGKKKPV-LAELLAELLAEL-[(VPGVG)<sub>2</sub>(VPGEG)<sub>10</sub>(VPGVG)<sub>2</sub>]-[VGIPG]<sub>60</sub>-VQEY-VYD-LFHAIHFIHGGWHGLHGWY-AVTDHPDRLWA-WERF-V.

**3.2. ELR Synthesis and Bioproduction.** The polymers were obtained in a yield of approximately 50 mg/L of bacterial culture. Their molecular weights and purity were confirmed by SDS-PAGE and MALDI-TOF, respectively. Moreover, the amino acid composition was confirmed by high-performance liquid chromatography (HPLC) and NMR. The results are shown in the [Supporting Information](#).

**3.3. Physical Characterization.** ELRs are characterized by a thermosensitive behavior that can be useful for performing controlled drug delivery, thus meaning that the self-assembling ability of ELRs makes them an interesting alternative for the development of biomedical devices. Consequently, the availability of ELR-based delivery systems with a  $T_t$  below the physiological temperature is extremely important for our purposes due to the fact that nanoparticles would be formed in the human body.<sup>42</sup>

The thermal behaviors of both ELRs were measured by DSC in PBS. As can be seen from [Table 1](#), both polymers were

**Table 1. Characterization of ELR Polymers<sup>a</sup>**

polymer	predicted molecular weight (Da)	experimental molecular weight (Da)	$T_t$ (°C)	endotoxin level (EU/mg)
control ELR	48 250	48 180	15.15	0.27
Akt-in ELR	55 330	55 540	14.58	0.25

<sup>a</sup>The experimental molecular weights were determined by MALDI-TOF/MS. Transition temperatures ( $T_t$ ) for polymers dissolved in PBS buffer (pH 7.4) were measured by differential scanning calorimetry (DSC).

found to behave as self-assembling smart systems with a  $T_t$  of approximately 15 °C, which corresponds to the transition of the hydrophobic block forming the nanoparticle core. These transition temperatures are very similar to those previously exhibited by amphiphilic blocks containing isoleucine and able to self-assemble into nanoparticles.<sup>34</sup> Interestingly, there are few differences between the  $T_t$  of both polymers despite their different compositions, thus meaning that the bioactive sequences added to the polymer carrying the Akt inhibitor do not affect their transition temperature. This means that they could be used for biomedical applications because at a body temperature of 37 °C, both ELR-based polymers self-assemble. Once the  $T_t$  of both polymers had been determined, nanoparticle formation had to be checked because the addition of bioactive sequences could prevent self-assembly of the polymers ([Table 2](#)).

The nanotechnological approach to cancer therapy takes advantage of the multiple abnormalities inherent to tumor vasculature, such as hypervascularization, aberrant vascular architecture, enhanced production of vascular permeability factors, and the lack of lymphatic drainage.<sup>20–22</sup> Thus, nanocarriers can selectively extravasate into tumor tissues

**Table 2. Characterization of ELR Nanoparticles<sup>a</sup>**

nanoparticle	size (nm)	PDI	$\zeta$ -potential (mV)	CMC	
				mg/mL	$\mu$ M
control NP	65.60 $\pm$ 3.73	0.087	-27.8 $\pm$ 1.5	0.25	4.49
Akt-in NP	72.46 $\pm$ 3.52	0.079	-26.2 $\pm$ 1.2	0.21	4.21

<sup>a</sup>Size and polydispersity index (PDI) of self-assembled polymers dissolved in PBS measured by dynamic light scattering (DLS). Surface charge of self-assembled polymers dissolved in ultrapure water type I measured by dynamic light scattering (DLS). The CMC was calculated from the surface tension using the pendant drop technique. Mean  $\pm$  SD.

due to their abnormal vascular nature and are subsequently not efficiently removed, thus remaining retained therein.<sup>43</sup> The ideal size for a nanoparticle depends on several factors. First of all, for significant extravasation from fenestrations in the tumor vasculature, nanocarriers need to be smaller than 400 nm.<sup>23</sup> Second, particles bigger than 200 nm are likely to be sensitive to macrophages and undergo opsonization.<sup>44</sup> As such, to avoid specific capture by the liver, they should be less than 100 nm in size<sup>45</sup> but larger than 10 nm to avoid filtration by the kidneys.<sup>46</sup> For all these reasons, nanoparticles with a size of 10–100 nm are preferred because of the enhanced permeability and retention (EPR) effect.<sup>23</sup> The EPR effect relies on the fact that tumors show abnormal vasculature, which means that nanosize drugs are accumulated in the tumors and show differential accumulation and therefore higher concentrations when compared to the plasma or other organs with proper vasculature. In our work, both polymers exhibited an ability to form nanoparticles, with an average size of 66 nm for the control polymer and 72 nm in the case of the Akt-in ELR, with low PDIs in both cases. This difference in size between the two nanoparticles is statistically relevant and bigger than for previous nanoparticles (55 nm) under the same conditions.<sup>34</sup> The size and morphology were corroborated by TEM, cryo-TEM, and fluorescence microscopy images (Figure 1A–C). As these previous nanocarriers consisted only of the amphiphilic ELR backbone, this difference with respect to our new nanoparticles is mainly due to the additional functional

peptides. To a lesser extent, the presence of the three bioactive sequences also results in a slight increase in the size of the Akt-in nanoparticles (72 nm). We can therefore conclude that both nanoparticles (control and those carrying the Akt inhibitor) meet all the size requirements for reaching the tumor in a controlled manner, as explained above. Furthermore, both control and Akt-in nanoparticles showed the same size when incubated with BSA (Table S2). This could mean that nanoparticles remain stable in systemic circulation and are not affected by plasmatic protein, such as albumin.

The critical micellar concentration (CMC) was also studied to determine the concentration above which ELRs self-assemble into nanoparticles. The pendant drop method showed that both polymers have their CMCs in PBS buffer between 0.21 mg/mL (4.21  $\mu$ M) for nanoparticles carrying the Akt inhibitor and 0.25 mg/mL (4.49  $\mu$ M) for control nanoparticles, as shown in Supporting Information Figure S7. This difference again highlights the fact that the presence of bioactive sequences does not affect the association and self-assembling ability of ELR-based nanoparticles. Experimental measurements are shown in the Supporting Information (Figures S4–S7).

The surface charge of nanoparticles is of marked importance regarding the electrostatic interactions between nanoparticles and the cellular membrane and for evaluating nanoparticle stability. Due to the negative component of the cellular membrane, cationic particles are typically preferred to nonspecifically enter cells by generating holes and inducing local disorders in the membrane,<sup>47</sup> whereas anionic particles strongly influence membrane structures.<sup>48</sup> However, anionic and neutral nanoparticles are thought to enter cells via endocytic pathways. Moreover, positively charged nanoparticles result in membrane depolarization, which reduces the viability of normal cells, thus having a stronger disruptive ability on the lipid bilayer of the cellular membrane.<sup>49</sup> Furthermore, neutral and negatively charged nanoparticles are able to enter the lymphatic system better than cationic carriers, which are more likely to form aggregates with interacting proteins, whereas neutral and anionic particles are thought to avoid renal clearance more efficiently.<sup>50</sup> The  $\zeta$ -

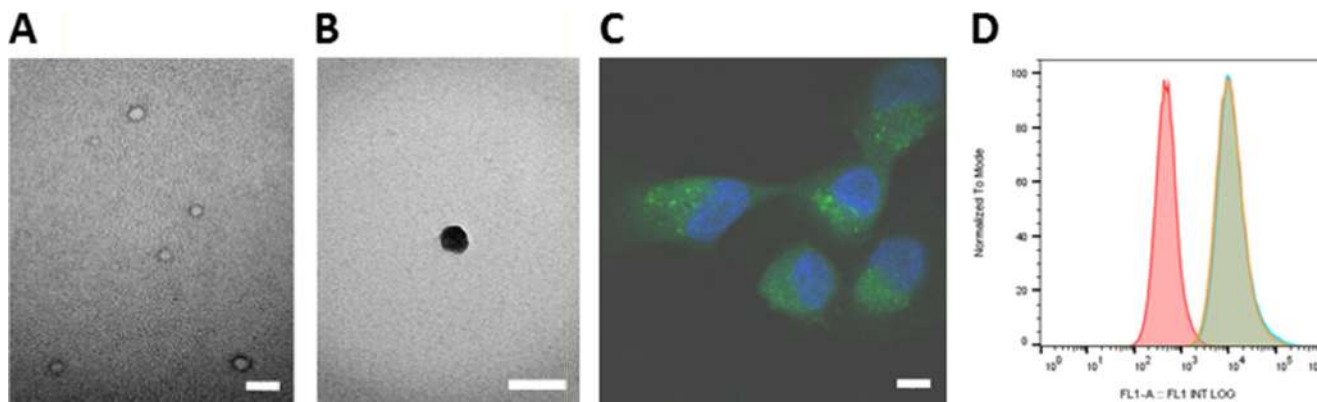


**Figure 1.** Characterization of ELR nanoparticles. TEM images of self-assembled nanoparticles stained with 1% uranyl acetate. (A) TEM images of self-assembled nanoparticles stained with 1% uranyl acetate. (B) cryo-TEM images of self-assembled nanoparticles stained with 1% uranyl acetate. (C) Confocal microscopy images of MDA-MB-231 cells incubated with self-assembled fluorescein-labeled nanoparticles. Cell nuclei were stained with DAPI. Scale bars: 100 nm for (A) and (B) and 2  $\mu$ m for (C). (D) Flow cytometry analysis of MDA-MB-231 cells incubated with fluorescein-labeled nanoparticles. The cell count was plotted as a function of FL1, which corresponded to the FITC channel for cells containing fluorescent nanoparticles (horizontal axis) against the number of events detected (vertical axis). Negative control untreated cells are plotted in red, whereas cells treated with control and Akt-in nanoparticles are shown in blue and orange, respectively.

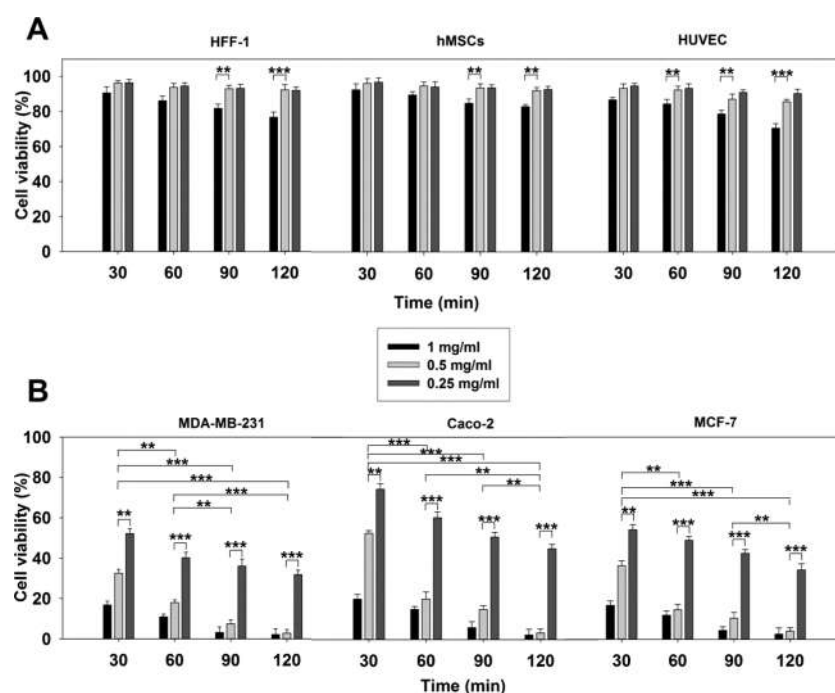


**Figure 2.** Percentage viabilities for HFF-1, hMSCs, and HUVEC (panel A) and MDA-MB-231, Caco-2, and MCF-7 (panel B) with respect to untreated cells. Cells were incubated with Akt-in nanoparticles at three concentrations and times, and viability was measured using the LIVE/DEAD assay kit.  $n = 3$  independent experiments, mean  $\pm$  SD. \*\* $p < 0.01$ ; \*\*\* $p < 0.001$ .

potential, which determines the surface charge of the nanoparticles, was found to be clearly negative ( $-27$  mV) due to the presence of glutamic acid residues at the nanoparticle surface. Despite the presence of three lysine residues in the corona, the  $\zeta$ -potential was not altered when compared to previous nanoparticles containing the same amphiphilic backbone reported by García-Arévalo et al.<sup>34</sup> Thus, these three lysine residues did not affect the nonspecific internalization of nanoparticles by electrostatic interactions with the cellular membrane. Moreover, the bioactive sequences of nanoparticles carrying the Akt inhibitor did not alter the  $\zeta$ -potential compared to control nanoparticles containing the ELR amphiphilic backbone, thus suggesting that bioactive domains are located at the nanoparticle core.

Flow cytometry analysis determined that both control and Akt-in nanoparticles were internalized in the same rate (Figure 1D) as both flow cytometry profiles overlapped (blue and orange). Thus, the slightly different size and  $\zeta$ -potential did not affect the cellular uptake of ELR-based nanoparticles.

Interestingly, both ELR-based nanoparticles showed a stable  $\zeta$ -potential when incubated with BSA (Table S2). This could mean that nanoparticles did not interact with albumin, which is the main protein in the plasma, and remained stable in systemic circulation.

**3.4. Effect of Nanoparticles on Cell Viability.** The main objective of this work was to develop a novel smart drug-delivery system to achieve an accurate release of an Akt inhibitor, which was designed to trigger apoptosis-mediated death of cancerous cells. Thus, based on different expression levels of Akt protein between cancerous and normal cells, the ELR-based nanoparticles were expected to show enhanced effect on cell viability of cancerous cells compared to normal ones. Once the nanoparticles had been physically characterized, their biological effects on three human cancer cell lines (Caco-2 epithelial colon carcinoma, and two breast cancer

lines MCF-7 and MDA-MB-231) and three normal human primary cell lines (HFF-1 fibroblasts, hMSCs (mesenchymal stem cells), and HUVEC endothelial cells) were examined. Human cancer cell lines were used for this purpose because of their higher expression of Akt protein than normal human cell lines. Furthermore, cancer cells are known to show higher internalization rates due to their faster metabolic state. We used three different concentrations of nanoparticles ranging from the critical micellar concentration (CMC) of 0.25–1 mg/mL. As shown in Figures 2 and S8, the viability of cells exposed to three different concentrations of both types of particles was studied at increasing incubation times. First of all, we determined the cytotoxic effect of control nanoparticles (Figure S8). Although this type of nanoparticle did not carry any bioactive sequence, internalization could affect cellular viability by destabilizing the membrane. Incubation with control nanoparticles did not significantly affect the viability of any of the six cell lines studied. Indeed, the results showed no difference either between the three different concentrations studied or between the different time points (from 30 to 120 min). Thus, we can conclude that, under the experimental conditions used, the control system does not cause a decrease in the viability of either cancerous or noncancerous cells. This lack of effect could happen either because control nanoparticles are not internalized or because they do not affect cell viability. As both types of nanoparticles have the same surface components, we expected the same internalization rates, thus meaning that we can conclude that control nanoparticles do not compromise cell viability as no detectable effect was observed.

Akt-in nanoparticles also showed no effect on the viability of noncancerous human cells at lower concentrations (Figures 2 and 3). Thus, endothelial cells, mesenchymal cells, and fibroblasts were only slightly affected when incubated for 120 min with nanoparticles at the highest concentration (1 mg/

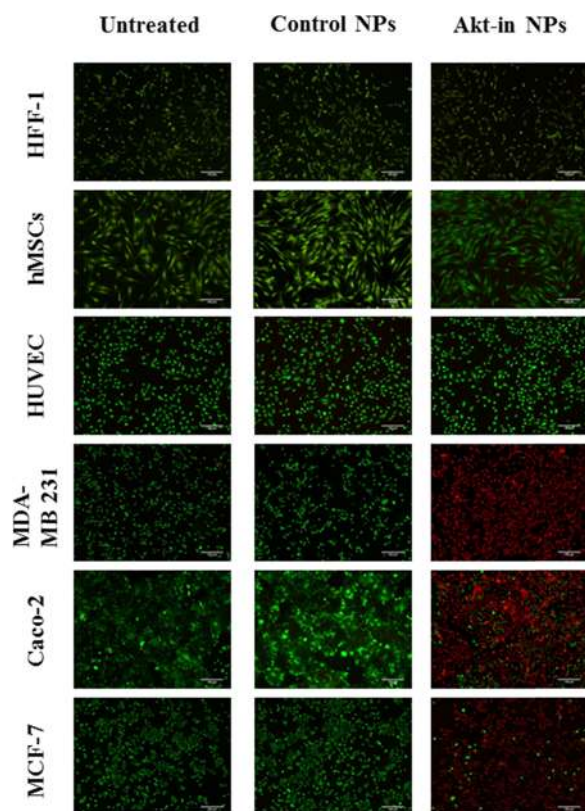


**Figure 3.** Representative fluorescence microscopy images for HFF-1, hMSCs, HUVEC, MDA-MB-231, Caco-2, and MCF-7 cells after incubation with control nanoparticles or Akt-in nanoparticles. Cells were incubated with Akt-in nanoparticles 0.5 mg/mL for 120 min, and viability was measured using the LIVE/DEAD assay kit. Scale bars are 100  $\mu\text{m}$ .

mL), with cell viabilities decreasing to 71, 83, and 77%, respectively. Furthermore, there were no significant differences between noncancerous cells treated with 0.25 and 0.5 mg/mL nanoparticles carrying the Akt inhibitor at any time. Of the three normal cell lines used, HUVEC cells were the most affected. In addition, vascular cells are the most exposed healthy cells due to their contact with nanoparticles during systemic administration.<sup>51</sup> In light of the above, we have provided evidence that the effect of nanoparticles on cell viability is both time- and concentration-dependent. Indeed, there were no significant differences between the viabilities of normal cells with concentrations of 0.25 and 0.5 mg/mL at any time point.

Cell proliferation was analyzed to determine the effect of our novel biomaterial when noncancerous cells were incubated with smart ELR nanoparticles (Supporting Information Figure S10). Thus, human fibroblasts (HFF-1), mesenchymal stem cells (hMSCs), and endothelial cells (HUVEC) were treated with ELR nanoparticles at 1 and 0.5 mg/mL for 72 h. First of all, control nanoparticles did not affect cellular proliferation of any of the three noncancerous cell lines compared to untreated cells. Interestingly, when HFF-1, hMSCs, and HUVEC cell lines were incubated with Akt-in nanoparticles, a slight effect was observed at early time points, but after the first 24 h, noncancerous cells were able to proliferate at the same rate as untreated cells. These results could mean that most of the cells surviving to treatment with Akt-in nanoparticles normally proliferated.

In contrast, when cancer cell lines were incubated with nanoparticles carrying the detachable Akt inhibitor, cell viability was strongly affected (Figure 2). Thus, the viability of cancer cells decreased to less than 20 and 40% after incubation with 0.5 and 1 mg/mL for only 30 min, respectively, thus indicating the rapid internalization of these Akt-in NPs. After incubation for 120 min, the minimal dose tested, which also corresponds to the CMC of the nanoparticles (Figure 2B), resulted in the death of 55–65% of cancerous cells. Similarly, when the nanoparticle concentrations were increased to 0.5 and 1 mg/mL, the effect on cancer cells was markedly higher (cell viabilities of 4 and 8%, respectively). Thus, an increase in the concentration of Akt-in nanoparticles results in a marked reduction in cell survival. This result suggests that this concentration is the minimal dose able to affect 50% cell viability. These findings also show that of the three cancer cell lines studied, Caco-2 cells are more resistant to treatment with nanoparticles. These differences could be due to the fact that these cell lines have different internalization rates. Interestingly, the 0.5 mg/mL concentration strongly affected the viability of cancer cells without affecting normal cells; therefore, this intermediate concentration was used for subsequent experiments because it seemed to be the largest therapeutic window in which significant differences in the viability of normal cells when compared to cancerous cells were observed. This is of particular importance as it could allow control by modulating the concentration. The enhanced action of nanoparticles on cancer cell lines when compared to normal cell lines could also be due to the fact that cancer cells are better able to internalize nanoparticles, as demonstrated by Villanueva et al.<sup>52</sup>

**3.5. Inhibition of Akt Phosphorylation.** Akt kinase is activated, in response to multiple stimuli, such as growth factors, by phosphatidyl inositol triphosphate products generated by PI3K. These lipid products bind to Akt and induce a conformational change in Akt, thus allowing PDK1 to phosphorylate threonine 308. Moreover, phosphorylation of serine 473 and membrane anchoring are required after threonine 308 phosphorylation for final activation of Akt kinase.<sup>28</sup> As we explained above, the mechanism of action of the small peptide inhibitor involved attachment to the Akt kinase, thereby avoiding the phosphorylation of Ser473.<sup>30</sup> To confirm the specific effect of the peptide inhibitor, immunoblotting assays were performed in Caco-2 and MDA-MB-231 cells after treatment with Akt-in nanoparticles for 2 h at 37 °C. As can be seen from Figure 4, Akt phosphorylation was not altered when cancer cell lines were incubated with control nanoparticles. However, when both cell lines were treated with nanoparticles carrying the inhibitor, phosphorylation of Akt protein at Ser473 was prevented. Consequently, we can conclude that the effect of Akt-in nanoparticles on cell viability is due to the accurate inhibitor delivery and its consequent antiphosphorylation activity, as expected.

**3.6. Apoptotic Death Triggered by Nanoparticles.** As shown above, ELR nanoparticles were able to provoke cancer cell death under the conditions tested; therefore, the next step was to determine the death pathway provoked. There are two major types of cell deaths: necrosis and apoptosis. Different diseases, including cancer, deregulate this apoptotic process, thereby resulting in pathological conditions.<sup>53</sup> For this reason, analysis of the signaling pathways that control apoptosis is of great importance for drug discovery and for investigating their therapeutic potential. Akt kinase plays a key role in several

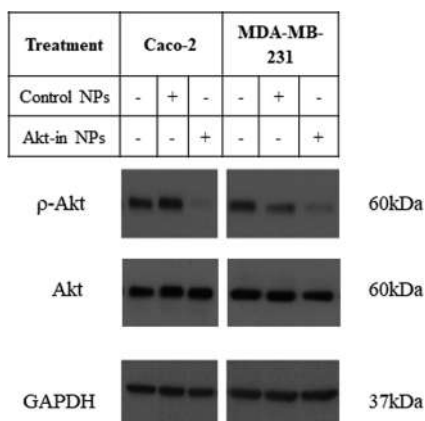


**Figure 4.** Inhibition of Akt phosphorylation triggered by nanoparticles in MDA-MB-231 and Caco-2 cell lines. Cells were incubated with control and Akt-in nanoparticles, and an immunoblot was performed to measure Akt phosphorylation at Ser473, total Akt, and glyceraldehyde 3-phosphate dehydrogenase (GAPDH) expressions, which was used as the load control.

multiple signaling pathways involving antiapoptotic effects.<sup>26</sup> Thus, upon blocking Akt kinase, cells should follow the apoptotic pathway and die. Hiromura et al.<sup>30</sup> demonstrated that Akt-in compromised Akt-dependent cellular proliferation and the antiapoptosis role of Akt. For that reason, apoptotic and necrotic cell percentages were determined in Caco-2 and MDA-MB-231 cells after treatment with nanoparticles carrying Akt-in for 2 h at 37 °C. As Figure 5 shows, apoptosis was the

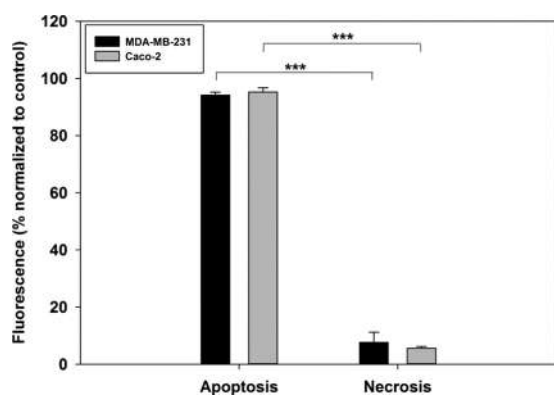


**Figure 5.** Cell-death pathways triggered by nanoparticles in MDA-MB-231 and Caco-2 cell lines. Cells were incubated with the nanoparticles carrying the Akt inhibitor, and an apoptosis/necrosis assay was performed for all samples. H<sub>2</sub>O<sub>2</sub> and Triton X-100-treated cells were considered as 100% apoptosis and necrosis control, respectively.  $n = 3$  independent experiments, mean  $\pm$  SD. \*\*\* $p < 0.001$ .

most commonly triggered death pathway for both cancer cell lines. The experiment with Caco-2 cells showed that 95% of the cells were in an apoptotic state and only 5% of dead cells in a necrotic state, whereas the experiment with MDA-MB-231 breast cancer cells confirmed that most cells died by apoptosis (93%) instead of necrosis (7%).

Thus, both cancer cell lines corroborated that the Akt inhibitor unlocked the apoptotic pathway blocked by Akt kinase. This is of particular importance as it shows that our ELR-based nanoparticles enhance the apoptotic pathway instead of being a toxic agent for cells.

**3.7. Endocytic Internalization of Nanoparticles.** Once the specificity of the Akt-in nanoparticles in cancer cell lines had been assessed, their internalization pathway was studied. In general, the internalization pathway for nanoparticles occurs via two mechanisms: phagocytosis and endocytosis.<sup>54</sup> As mentioned above, larger nanoparticles (200 nm) are more likely to undergo phagocytosis, whereas smaller ones enter cells by endocytosis. Three different types of endocytosis have been described: macropinocytosis, clathrin-mediated endocytosis, and caveolae-mediated endocytosis,<sup>38</sup> but only the latter two mechanisms work via receptor–ligand interactions forming vesicles that are invaginated, such as endosomes and lysosomes.<sup>38,55,56</sup> In our case, internalization of the NPs via an endocytic mechanism is critical to allow the Akt inhibitor to reach the cytoplasm after the participation of the lysosomal enzyme cathepsin D and the H5 peptide for endolysosomal escape. Of the six cell lines used above, Caco-2 and MDA-MB-231 were selected to determine the internalization pathway due to their higher levels of Akt expression and the different activities of the Akt-in nanoparticles observed. This selection could give us a better insight into the accuracy and mechanism of action of the nanoparticles when faced with cancer cells in which Akt kinase is overexpressed. As such, this selection could be the most realistic in vitro scenario for our study prior to using in vivo models in future studies. To determine this, Caco-2 and MDA-MB-231 cells were pretreated with four different endocytosis inhibitors for 30 min at 37 °C and then incubated with Akt-in nanoparticles for 2 h at 37 °C. Maximum viability (positive control) was achieved when cells were treated with PBS for 2 h, whereas the negative control was achieved with Akt-in NPs instead of PBS. As can be seen from Figures 6 and 7, the inhibition of macro-

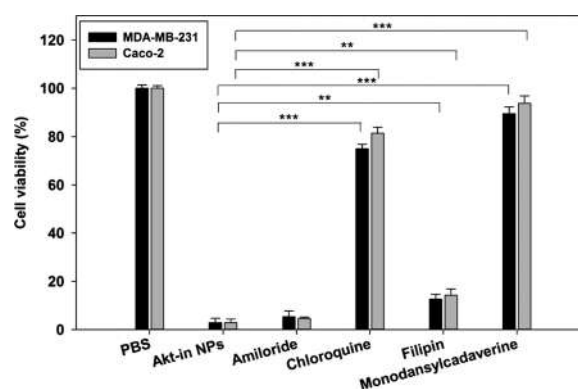


**Figure 6.** Study of the internalization pathways for nanoparticles carrying the Akt inhibitor in MDA-MB-231 and Caco-2 cell lines. Cells were incubated with PBS and 0.5 mg/mL Akt-in nanoparticles or preincubated with an internalization inhibitor, such as amloride, chloroquine, filipin, or monodansylcadaverine prior to treatment with 0.5 mg/mL Akt-in nanoparticles. Viability was measured using the LIVE/DEAD assay kit.  $n = 3$  independent experiments, mean  $\pm$  SD. \*\* $p < 0.01$ ; \*\*\* $p < 0.001$ .

pinocytosis by amloride (Na<sup>+</sup>/H<sup>+</sup> exchange) did not alter the effect of nanoparticles on cell viability, whereas the inhibition of caveolae-mediated endocytosis by filipin only showed a minimum but statistically significant effect (14% cell viability). However, the inhibition of clathrin-mediated endocytosis by monodansylcadaverine was found to almost completely inhibit the action of nanoparticles, and a cell viability of 92% was restored. Additionally, the inhibition of acidification in acidic

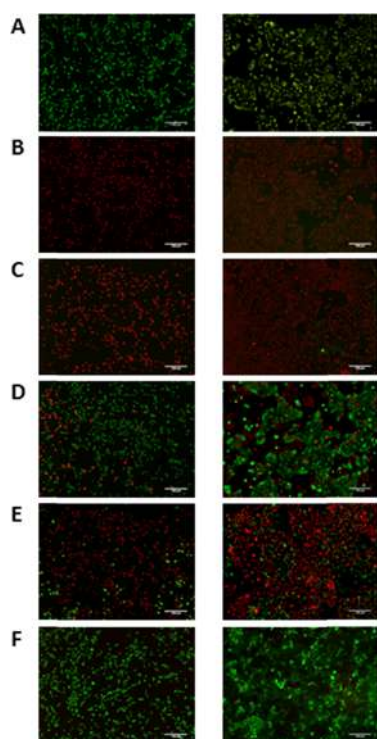


**Figure 7.** Representative fluorescence microscopy images for Caco-2 (right) and MDA-MB-231 (left) after incubation with (A) PBS (100% viability) and (B) 0.5 mg/mL Akt-in nanoparticles (0% viability) or preincubated with an internalization inhibitor, such as (C) amiloride, (D) chloroquine, (E) filipin, or (F) monodansylcadaverine prior to treatment with Akt-in nanoparticles. Cells were incubated with endocytosis inhibitors for 30 min before the treatment with Akt-in nanoparticles 0.5 mg/mL for 120 min, and viability was measured using the LIVE/DEAD assay kit. Scale bars are 100  $\mu$ m.

vesicles by chloroquine also significantly affected (80% cell viability) the action of nanoparticles.

These findings show the primary influence of clathrin-mediated endocytosis for the internalization of nanoparticles due to the action of the enzyme cathepsin D on the CatD-sensitive sequence to release the Akt inhibitor. We have also demonstrated the importance of endosomal/lysosomal acidification for our nanoparticles as this acidification allows the conformational change and action of H5 peptide to escape from acidic vesicles. All these results may also suggest that lysosomes are key actors in the intracellular activation of nanoparticles because if the nanoparticles underwent a different internalization pathway they would not be effective.

**3.8. Intracellular Nanoparticle Activation.** One of the most promising advantages of genetically engineered ELR-based nanoparticles is the fact that the action on targeted cells and tissues can be modulated by adding different bioactive functionalities. As shown above, endocytic acidification seemed to be a key factor in nanoparticle activation. Endosome acidification upon fusion with the lysosome also means that multiple degradative enzymes act on the cargo.<sup>57</sup> One of the key lysosomal proteases is the aspartyl endopeptidase cathepsin D,<sup>58</sup> which shows a higher expression in tumors than in normal tissues and is thought to promote tumor invasion and growth.<sup>40</sup> As such, we included a CatD-sensitive sequence upstream of Akt-in in our polymer to allow the inhibitor to be removed from the NP and be released into the cytoplasm after the action of H5 for lysosomal escape, thereby

binding to the targeted protein. Thus, as the participation of CatD-directed degradation should be critical for Akt-in activation, we assessed the role of CatD in our system by selectively inhibiting it using Pepstatin A.<sup>59</sup> As such, we hypothesized that when the lysosomal degradative enzyme cathepsin D is inhibited, the Akt inhibitor peptide cannot be released into the cytoplasm and reach Akt protein to block it. The two human cancer cell lines Caco-2 and MDA-MB-231 cells were preincubated with 100  $\mu$ M of Pepstatin A for 16 h at 37  $^{\circ}$ C before treatment with Akt-in nanoparticles for 2 h at 37  $^{\circ}$ C. The cell viability was then assessed. As can be seen from Figure 8, incubation of cells with the CatD inhibitor did not

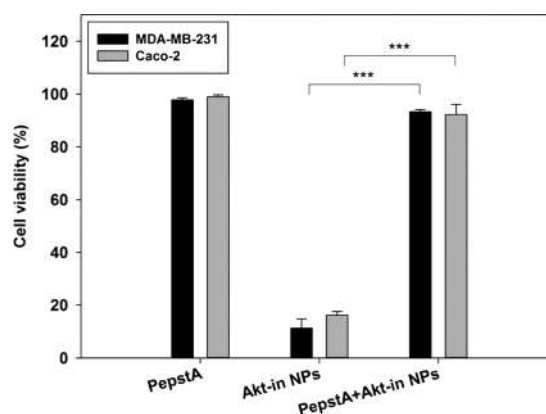


**Figure 8.** Lysosomal trafficking of nanoparticles carrying the Akt inhibitor in MDA-MB-231 and Caco-2 cell lines. Cells were incubated with Pepstatin A (negative control), Akt-in nanoparticles, or both, and viability was measured using the LIVE/DEAD assay kit.  $n = 3$  independent experiments, mean  $\pm$  SD. \*\*\* $p < 0.001$ .

produce any effect on cell viability despite blocking an important degradative enzyme. Similarly, when cells were pretreated with Pepstatin A, the nanoparticles also had no effect and cell viability was not affected, in contrast to the effect of nanoparticles in both these cancer cell lines when the action of CatD is not inhibited. We can therefore conclude that Akt-in nanoparticles lose their effect on cell viability when their intracellular activation is inhibited. This could be due to the fact that the peptide is unable to escape from the lysosome, thus meaning that Akt protein is not reached and continues to enhance cell proliferation and block apoptotic cell death.

#### 4. CONCLUSIONS

One of the disadvantages of current chemotherapeutic treatments against cancer is the lack of specificity of the drugs, which therefore results in significant damage to healthy tissues.<sup>25</sup> To improve the selectivity of new drugs, nanotechnological approaches with incorporated targeting systems appear to be the best strategy.<sup>2</sup> Furthermore, different types of solid tumors offer multiple obstacles to the drug-delivery systems tested to date. Akt kinase is one of the most interesting of the multiple proteins that can be targeted due to its higher expression in cancerous cells and its role as a key factor controlling multiple signaling pathways and processes, such as cell growth, proliferation, and survival.<sup>26</sup> The small peptide inhibitor Akt-in was therefore designed to block Akt protein, thereby inhibiting both its essential activity and tumor cell growth.<sup>30</sup>

Thus, we have developed a new smart nanodevice specifically designed including different bioactive peptides so as to achieve the proper delivery of therapeutic agents in targeted cells and tissues. Genetic-engineering techniques used for the design of these ELR polymers allow us to be able to create different advanced drug-delivery systems with diverse applications as a therapeutic approach for multiple diseases, taking advantage of its smart stimuli-responsive behavior. In this work, we have developed a new ELR-based nanoparticle carrying a small peptide inhibitor against Akt protein to create an advanced approach for application thereof in the therapeutic treatment of cancer. It should be noted that a complex design of the smart nanoparticles, with different actors, was needed to successfully release the inhibitor into the cell cytoplasm, thereby avoiding degradative proteases, which would not allow the peptide to enter otherwise.

We tested the specificity of this novel ELR nanoparticle in 6 different cell lines. Thus, our drug-delivery system showed no effect in three primary noncancerous cell lines, whereas the same treatment showed lethal effects in breast and colorectal cancerous cells. Moreover, *in vitro* experiments confirmed that each block included in the polymer was absolutely required for the proper release of the inhibitor in the cellular cytoplasm. Thus, in activation of lysosomal proteases and inhibition of vesicle acidification resulted in abolished effects of nanoparticles.

Overall, based on our findings, we can conclude that this smart nanodevice could be a novel strategy for the proper release of therapeutic agents at the molecular level in targeted cells. This study is the first to report an accurate smart nanodevice against Akt protein after intracellular activation. Interestingly, our system improved the accuracy of the inhibitor in a time- (our system was 12 times faster than the inhibitor alone) and dose-dependent manner (5 times lower amount of inhibitor), compared to previous works with Akt-in.<sup>30</sup> This improved action of Akt-in when carried in nanoparticles could be due to the better internalization of nanoparticles compared to nude peptides and their shielding effect, which protects the inhibitor from cellular proteases.

It is worthy to mention that our new therapeutic system is not limited to one type of cancer as it is targeted to Akt kinase protein, which is overexpressed in multiple neoplastic diseases, such as colon, pancreatic, breast, ovarian, and lung cancers. Further studies are needed to study the accuracy of these nanoparticles in *in vivo* models better resembling the tumor environment and its interactions with nanocarriers. In the future, patients overexpressing Akt may be candidates for therapeutic treatment with nanoparticles bearing the inhibitor, which could improve the problems caused by current nonspecific chemotherapeutic drugs.

## ■ ASSOCIATED CONTENT

### ● Supporting Information

The Supporting Information is available free of charge on the ACS Publications website at DOI: [10.1021/acs.biomac.9b00206](https://doi.org/10.1021/acs.biomac.9b00206).

Amino acid sequence of polymers (Table S1), SDS-PAGE of ELRs purification (Figure S1), high-performance liquid chromatography (HPLC) and mass spectrometry (MALDI-TOF/MS) analyses of the control polymer (Figure S2) and the Akt-in polymer (Figure S3), differential scanning calorimetry (DSC) analysis of

ELRs (Figure S4), dynamic light scattering analysis of nanoparticle size (Figure S5), dynamic light scattering analysis of nanoparticle  $\zeta$ -potential (Figure S6), dynamic light scattering analysis of nanoparticle size and  $\zeta$ -potential after incubation with 5% BSA (Table S2), critical micellar concentration (CMC) analysis of ELRs using the pendant drop method (Figure S7) and LIVE/DEAD analysis of HFF-1, hMSCs, HUVEC, MDA-MB-231, Caco-2, and MCF-7 incubated with control nanoparticles at three concentrations and times (Figure S8) (PDF)

## ■ AUTHOR INFORMATION

### Corresponding Author

\*E-mail: [arias@bioforge.uva.es](mailto:arias@bioforge.uva.es).

### ORCID

Juan Gonzalez-Valdivieso: [0000-0001-9007-2312](https://orcid.org/0000-0001-9007-2312)

J. Carlos Rodriguez-Cabello: [0000-0002-3438-858X](https://orcid.org/0000-0002-3438-858X)

F. Javier Arias: [0000-0001-8584-3768](https://orcid.org/0000-0001-8584-3768)

### Notes

The authors declare no competing financial interest.

## ■ ACKNOWLEDGMENTS

The authors are grateful for financial support from the European Social Fund (ESF) and the European Regional Development Fund (ERDF), as well as funding from the EU (NMP-2014-646075), the MINECO (PCIN-2015-010, MAT2015-68901-R, MAT2016-79435-R, and MAT2016-78903-R), the JCyL (project VA317P18), the CIBER-BBN, the JCyL, and the Instituto de Salud Carlos III under the “Network Center of Regenerative Medicine and Cellular Therapy of Castilla and Leon”. The authors would like to thank R. Garcia for her technical assistance.

## ■ REFERENCES

- (1) Saxena, R.; Nanjan, M. J. Elastin-like polypeptides and their applications in anticancer drug delivery systems: a review. *Drug Delivery* **2015**, *22*, 156–167.
- (2) Jain, V.; Jain, S.; Mahajan, S. C. Nanomedicines based drug delivery systems for anti-cancer targeting and treatment. *Curr. Drug Delivery* **2015**, *12*, 177–191.
- (3) Zhang, Y.; Chan, H. F.; Leong, K. W. Advanced materials and processing for drug delivery: the past and the future. *Adv. Drug Delivery Rev.* **2013**, *65*, 104–120.
- (4) Han, W.; Chilkoti, A.; Lopez, G. P. Self-assembled hybrid elastin-like polypeptide/silica nanoparticles enable triggered drug release. *Nanoscale* **2017**, *9*, 6178–6186.
- (5) Shi, J.; Kantoff, P. W.; Wooster, R.; Farokhzad, O. C. Cancer nanomedicine: progress, challenges and opportunities. *Nat. Rev. Cancer* **2017**, *17*, 20–37.
- (6) Raucher, D.; Massodi, I.; Bidwell, G. L. Thermally targeted delivery of chemotherapeutics and anti-cancer peptides by elastin-like polypeptide. *Expert Opin. Drug Delivery* **2008**, *5*, 353–369.
- (7) Floss, D. M.; Schallau, K.; Rose-John, S.; Conrad, U.; Scheller, J. Elastin-like polypeptides revolutionize recombinant protein expression and their biomedical application. *Trends Biotechnol.* **2010**, *28*, 37–45.
- (8) Shi, P.; Gustafson, J. A.; MacKay, J. A. Genetically engineered nanocarriers for drug delivery. *Int. J. Nanomed.* **2014**, *9*, 1617–1626.
- (9) Ryu, J. S.; Raucher, D. Elastin-like polypeptide for improved drug delivery for anticancer therapy: preclinical studies and future applications. *Expert Opin. Drug Delivery* **2015**, *12*, 653–667.
- (10) Rodríguez-Cabello, J. C.; Pina, M. J.; Ibanez-Fonseca, A.; Fernandez-Colino, A.; Arias, F. J. Nanotechnological Approaches to

Therapeutic Delivery Using Elastin-Like Recombinamers. *Bioconjug Chem.* **2015**, *26*, 1252–1265.

(11) Rodriguez-Cabello, J. C.; Arias, F. J.; Rodrigo, M. A.; Girotti, A. Elastin-like polypeptides in drug delivery. *Adv. Drug Delivery Rev.* **2016**, *97*, 85–100.

(12) Arias, F. J.; Santos, M.; Ibanez-Fonseca, A.; Pina, M. J.; Serrano, S. Elastin-Like Recombinamers As Smart Drug Delivery Systems. *Curr. Drug Targets* **2018**, *19*, 360–379.

(13) Fernández-Colino, A.; Quinteros, D. A.; Allemandi, D. A.; Girotti, A.; Palma, S. D.; Arias, F. J. Self-Assembling Elastin-Like Hydrogels for Timolol Delivery: Development of an Ophthalmic Formulation Against Glaucoma. *Mol. Pharm.* **2017**, *14*, 4498–4508.

(14) Mastria, E. M.; Chen, M.; McDaniel, J. R.; Li, X.; Hyun, J.; Dewhirst, M. W.; Chilkoti, A. Doxorubicin-conjugated polypeptide nanoparticles inhibit metastasis in two murine models of carcinoma. *J. Controlled Release* **2015**, *208*, 52–58.

(15) MacKay, J. A.; Chen, M.; McDaniel, J. R.; Liu, W.; Simnick, A. J.; Chilkoti, A. Self-assembling chimeric polypeptide-doxorubicin conjugate nanoparticles that abolish tumours after a single injection. *Nat. Mater.* **2009**, *8*, 993–999.

(16) McDaniel, J. R.; Callahan, D. J.; Chilkoti, A. Drug delivery to solid tumors by elastin-like polypeptides. *Adv. Drug Delivery Rev.* **2010**, *62*, 1456–1467.

(17) Pina, M. J.; Alex, S. M.; Arias, F. J.; Santos, M.; Rodriguez-Cabello, J. C.; Ramesan, R. M.; Sharma, C. P. Elastin-like recombinamers with acquired functionalities for gene-delivery applications. *J. Biomed. Mater. Res., Part A* **2015**, *103*, 3166–3178.

(18) Hillaireau, H.; Couvreur, P. Nanocarriers' entry into the cell: relevance to drug delivery. *Cell Mol. Life Sci.* **2009**, *66*, 2873–2896.

(19) Bae, H.; Chu, H.; Edalat, F.; Cha, J. M.; Sant, S.; Kashyap, A.; Ahari, A. F.; Kwon, C. H.; Nichol, J. W.; Manoucheri, S.; Zamanian, B.; Wang, Y.; Khademhosseini, A. Development of functional biomaterials with micro- and nanoscale technologies for tissue engineering and drug delivery applications. *J. Tissue Eng. Regen. Med.* **2014**, *8*, 1–14.

(20) Torchilin, V. P. Drug targeting. *Eur. J. Pharm. Sci.* **2000**, *11*, S81–S91.

(21) Matsumura, Y.; Maeda, H. A new concept for macromolecular therapeutics in cancer chemotherapy: mechanism of tumoritropic accumulation of proteins and the antitumor agent smancs. *Cancer Res.* **1986**, *46*, 6387–6392.

(22) Maeda, H.; Bharate, G. Y.; Daruwalla, J. Polymeric drugs for efficient tumor-targeted drug delivery based on EPR-effect. *Eur. J. Pharm. Biopharm.* **2009**, *71*, 409–419.

(23) Jain, R. K. Transport of molecules in the tumor interstitium: a review. *Cancer Res.* **1987**, *47*, 3039–3051.

(24) Piña, M. J.; Girotti, A.; Santos, M.; Rodriguez-Cabello, J. C.; Arias, F. J. Biocompatible ELR-Based Polyplexes Coated with MUC1 Specific Aptamers and Targeted for Breast Cancer Gene Therapy. *Mol. Pharm.* **2016**, *13*, 795–808.

(25) Byrne, J. D.; Betancourt, T.; Brannon-Peppas, L. Active targeting schemes for nanoparticle systems in cancer therapeutics. *Adv. Drug Delivery Rev.* **2008**, *60*, 1615–1626.

(26) Cantley, L. C. The phosphoinositide 3-kinase pathway. *Science* **2002**, *296*, 1655–1657.

(27) Bellacosa, A.; Testa, J. R.; Staal, S. P.; Tschlis, P. N. A retroviral oncogene, akt, encoding a serine-threonine kinase containing an SH2-like region. *Science* **1991**, *254*, 274–277.

(28) Vanhaesebroeck, B.; Alessi, D. R. The PI3K-PDK1 connection: more than just a road to PKB. *Biochem. J.* **2000**, *346*, 561–576.

(29) Luo, J.; Manning, B. D.; Cantley, L. C. Targeting the PI3K-Akt pathway in human cancer: rationale and promise. *Cancer Cell* **2003**, *4*, 257–262.

(30) Hiromura, M.; Okada, F.; Obata, T.; Auguin, D.; Shibata, T.; Roumestand, C.; Noguchi, M. Inhibition of Akt kinase activity by a peptide spanning the betaA strand of the proto-oncogene TCL1. *J. Biol. Chem.* **2004**, *279*, 53407–53418.

(31) Rodriguez-Cabello, J. C.; Girotti, A.; Ribeiro, A.; Arias, F. J. Synthesis of genetically engineered protein polymers (recombi-

namers) as an example of advanced self-assembled smart materials. *Methods Mol Biol.* **2012**, *811*, 17–38.

(32) Sallach, R. E.; Cui, W.; Balderrama, F.; Martinez, A. W.; Wen, J.; Haller, C. A.; Taylor, J. V.; Wright, E. R.; Long, R. C., Jr.; Chaikof, E. L. Long-term biostability of self-assembling protein polymers in the absence of covalent crosslinking. *Biomaterials* **2010**, *31*, 779–791.

(33) Fenton, O. S.; Olafson, K. N.; Pillai, P. S.; Mitchell, M. J.; Langer, R. Advances in Biomaterials for Drug Delivery. *Adv. Mater.* **2018**, *30*, No. 1705328.

(34) García-Arévalo, C.; Bermejo-Martin, J. F.; Rico, L.; Iglesias, V.; Martin, L.; Rodriguez-Cabello, J. C.; Arias, F. J. Immunomodulatory nanoparticles from elastin-like recombinamers: single-molecules for tuberculosis vaccine development. *Mol. Pharm.* **2013**, *10*, 586–597.

(35) Kowalczyk, T.; Hnatuszko-Konka, K.; Gerszberg, A.; Kononowicz, A. K. Elastin-like polypeptides as a promising family of genetically-engineered protein based polymers. *World J. Microbiol. Biotechnol.* **2014**, *30*, 2141–2152.

(36) MacEwan, S. R.; Chilkoti, A. Applications of elastin-like polypeptides in drug delivery. *J. Controlled Release* **2014**, *190*, 314–330.

(37) Santos, M.; Serrano-Ducar, S.; Gonzalez-Valdivieso, J.; Vallejo, R.; Girotti, A.; Cuadrado, P.; Arias, F. J. Genetically Engineered Elastin-based Biomaterials for Biomedical Applications. *Curr. Med. Chem.* **2018**, No. 25.

(38) Sahay, G.; Alakhova, D. Y.; Kabanov, A. V. Endocytosis of nanomedicines. *J. Controlled Release* **2010**, *145*, 182–195.

(39) Ohmori, N.; Niidome, T.; Wada, A.; Hirayama, T.; Hatakeyama, T.; Aoyagi, H. The enhancing effect of anionic alpha-helical peptide on cationic peptide-mediated transfection systems. *Biochem. Biophys. Res. Commun.* **1997**, *235*, 726–729.

(40) Kirana, C.; Shi, H.; Laing, E.; Hood, K.; Miller, R.; Bethwaite, P.; Keating, J.; Jordan, T. W.; Hayes, M.; Stubbs, R. Cathepsin D Expression in Colorectal Cancer: From Proteomic Discovery through Validation Using Western Blotting, Immunohistochemistry, and Tissue Microarrays. *Int. J. Proteomics* **2012**, *2012*, No. 245819.

(41) Buré, C.; Maget, R.; Delmas, A. F.; Pichon, C.; Midoux, P. Histidine-rich peptide: evidence for a single zinc-binding site on H5WYG peptide that promotes membrane fusion at neutral pH. *J. Mass Spectrom.* **2009**, *44*, 81–89.

(42) Moktan, S.; Perkins, E.; Kratz, F.; Raucher, D. Thermal targeting of an acid-sensitive doxorubicin conjugate of elastin-like polypeptide enhances the therapeutic efficacy compared with the parent compound in vivo. *Mol. Cancer Ther.* **2012**, *11*, 1547–1556.

(43) Bouzin, C.; Feron, O. Targeting tumor stroma and exploiting mature tumor vasculature to improve anti-cancer drug delivery. *Drug Resist. Updates* **2007**, *10*, 109–120.

(44) Owens, D. E., 3rd; Peppas, N. A. Opsonization, biodistribution, and pharmacokinetics of polymeric nanoparticles. *Int. J. Pharm.* **2006**, *307*, 93–102.

(45) Khullar, O. V.; Griset, A. P.; Gibbs-Strauss, S. L.; Chiriac, L. R.; Zubris, K. A.; Frangioni, J. V.; Grinstaff, M. W.; Colson, Y. L. Nanoparticle migration and delivery of Paclitaxel to regional lymph nodes in a large animal model. *J. Am. Coll. Surg.* **2012**, *214*, 328–337.

(46) Davis, M. E.; Chen, Z. G.; Shin, D. M. Nanoparticle therapeutics: an emerging treatment modality for cancer. *Nat. Rev. Drug Discovery* **2008**, *7*, 771–782.

(47) Lin, J.; Zhang, H.; Chen, Z.; Zheng, Y. Penetration of lipid membranes by gold nanoparticles: insights into cellular uptake, cytotoxicity, and their relationship. *ACS Nano* **2010**, *4*, 5421–5429.

(48) Li, Y.; Gu, N. Thermodynamics of charged nanoparticle adsorption on charge-neutral membranes: a simulation study. *J. Phys. Chem. B* **2010**, *114*, 2749–2754.

(49) Arvizo, R. R.; Miranda, O. R.; Thompson, M. A.; Pabelick, C. M.; Bhattacharya, R.; Robertson, J. D.; Rotello, V. M.; Prakash, Y. S.; Mukherjee, P. Effect of nanoparticle surface charge at the plasma membrane and beyond. *Nano Lett.* **2010**, *10*, 2543–2548.

(50) Malam, Y.; Loizidou, M.; Seifalian, A. M. Liposomes and nanoparticles: nanosized vehicles for drug delivery in cancer. *Trends Pharm. Sci.* **2009**, *30*, 592–599.

(51) Spencer, D. S.; Puranik, A. S.; Peppas, N. A. Intelligent Nanoparticles for Advanced Drug Delivery in Cancer Treatment. *Curr. Opin. Chem. Eng.* **2015**, *7*, 84–92.

(52) Villanueva, A.; Canete, M.; Roca, A. G.; Calero, M.; Veintemillas-Verdaguer, S.; Serna, C. J.; Morales Mdel, P.; Miranda, R. The influence of surface functionalization on the enhanced internalization of magnetic nanoparticles in cancer cells. *Nanotechnology* **2009**, *20*, No. 115103.

(53) van Engeland, M.; Nieland, L. J.; Ramaekers, F. C.; Schutte, B.; Reutelingsperger, C. P. Annexin V-affinity assay: a review on an apoptosis detection system based on phosphatidylserine exposure. *Cytometry* **1998**, *31*, 1–9.

(54) Coco, R.; Plapied, L.; Pourcelle, V.; Jerome, C.; Brayden, D. J.; Schneider, Y. J.; Preat, V. Drug delivery to inflamed colon by nanoparticles: comparison of different strategies. *Int. J. Pharm.* **2013**, *440*, 3–12.

(55) Conner, S. D.; Schmid, S. L. Regulated portals of entry into the cell. *Nature* **2003**, *422*, 37–44.

(56) Gamboa, J. M.; Leong, K. W. In vitro and in vivo models for the study of oral delivery of nanoparticles. *Adv. Drug Delivery Rev.* **2013**, *65*, 800–810.

(57) Jovic, M.; Sharma, M.; Rahajeng, J.; Caplan, S. The early endosome: a busy sorting station for proteins at the crossroads. *Histol. Histopathol.* **2010**, *25*, 99–112.

(58) Pranjol, M. Z.; Gutowski, N.; Hannemann, M.; Whatmore, J. The Potential Role of the Proteases Cathepsin D and Cathepsin L in the Progression and Metastasis of Epithelial Ovarian Cancer. *Biomolecules* **2015**, *5*, 3260–3279.

(59) Amritraj, A.; Wang, Y.; Revett, T. J.; Vergote, D.; Westaway, D.; Kar, S. Role of cathepsin D in U18666A-induced neuronal cell death: potential implication in Niemann-Pick type C disease pathogenesis. *J. Biol. Chem.* **2013**, *288*, 3136–3152.

## Supplementary material

	<b>3K</b>	<b>LAEL</b>	<b>E<sub>50</sub></b>	<b>I<sub>60</sub></b>	<b>CatD</b>	<b>H5</b>	<b>Akt-in</b>
<b>Control</b>	MGKKKP V	(LAEL) <sub>3</sub>	[(VPGVG) <sub>2</sub> (VPGEG) <sub>10</sub> (VPGVG) <sub>2</sub> ]	[VGIPG] <sub>60</sub>	---	---	---
<b>Akt-in</b>	MGKKKP V	(LAEL) <sub>3</sub>	[(VPGVG) <sub>2</sub> (VPGEG) <sub>10</sub> (VPGVG) <sub>2</sub> ]	[VGIPG] <sub>60</sub>	VQEYVYD	LFHAI AHF HIHGGWH GLIHGWY	AVTDHP DRLWAW ERF

**Table S1.** Composition of polymers. Amino acid sequence of ELR polymers.

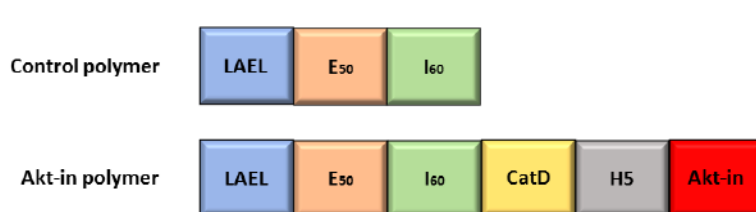


**Figure S1.** Composition of polymers. The different blocks forming ELR-based polymers. Non-scaled scheme.

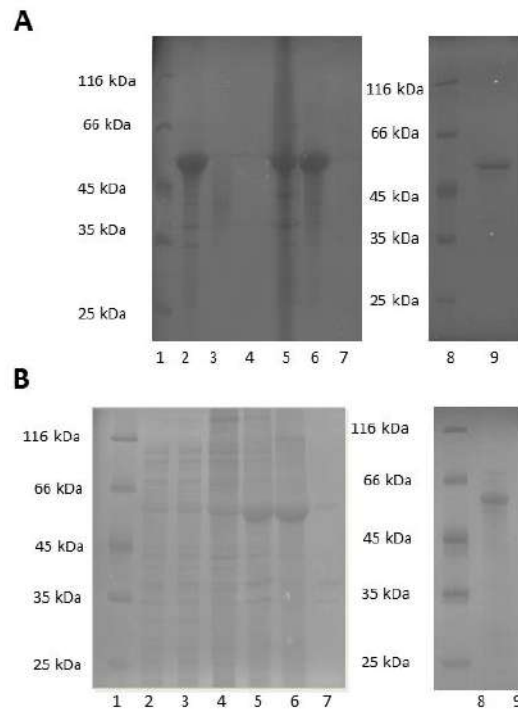
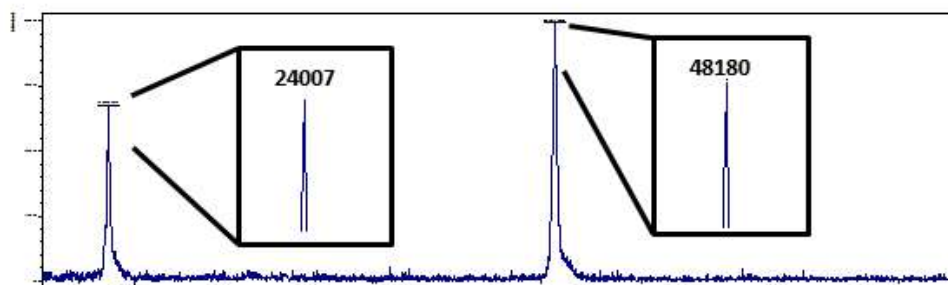


**Figure S2.** Characterization of ELR polymers. The expression vectors containing the selected ELR genes were transformed into *Escherichia coli* BLR (DE3) strain for production. The ELR was then bioproduced in *Escherichia coli* in a 15-L bioreactor and purified by several cooling and heating purification cycles (Inverse Transition Cycling) following centrifugation, thereby taking advantage of the ability of these recombinamers to aggregate above their transition temperature. Finally, the polymer was dialyzed against ultrapure water type I and sterilized by filtration (0.22  $\mu\text{m}$  filters). A: Purification of control polymer measured by SDS-PAGE. 1: protein marker; 2: cold supernatant; 3: cold pellet; 4: hot supernatant; 5: hot pellet; 6: cold supernatant; 7: cold pellet; 8: protein marker; 9: pure lyophilized polymer. B: Purification of Akt-in polymer measured by SDS-PAGE. 1: protein marker; 2: production sample; 3: production sample; 4: cold pellet; 5: cold supernatant; 6: hot pellet; 7: hot supernatant; 8: protein marker; 9: pure lyophilized polymer

**A**

	AA	Mr patron	Experimental		Theoretical
			% masa	count	count
D	ASP+ASN	133.11	0.00	0.00	
E	GLU+GLN	147.13	3.60	14,13	13
N		132.12	0.00	0.00	
S	SER	105.09	0.00	0.00	
Q		146.15	0.00	0.00	
H	HIS	151.9	0.00	0.00	
G	GLY	75.07	28.27	219,97	220
T	THR	119.12	0.00	0.00	
R	ARG	174.2	0.00	0.00	
A	ALA	89.1	0.80	5,17	3
Y	TYR	181.19	0.00	0.00	
C	CYS	240	0.00	0.00	
V	VAL	117.15	29.60	145,53	150
M	MET	149.21	0.00	0.00	
W	TRP	204.33	0.00	0.00	
F	PHE	165.19	0.00	0.00	
I	ILE	131.18	14.07	61,75	60
L	LEU	131,18	1,57	6,90	6
K	LYS	146.65	0.71	2,90	3
P	PRO	115.13	21,38	108,43	110
			100,00	564,77	565

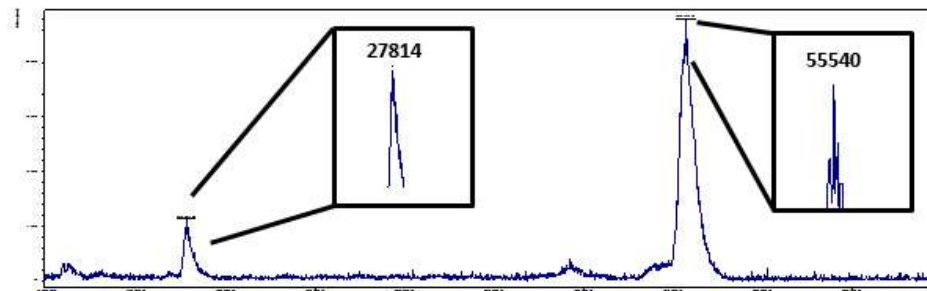
**B**



**Figure S3.** Characterization of control polymer. A: The amino acid composition was verified by high performance liquid chromatography (HPLC). B: The molecular weight of the recombinamer was determined by mass spectrometry (MALDI-TOF/MS). MALDI-TOF spectrum represents non-quantitative intensity (a.u.) against  $m/z$  (mass divided by net charge of the molecule) of the ELR. Either the mono charged either the doubly charged recombinamers were detected. The theoretical molecular weight was 48250 Da.

**A**

	AA	Mr patron	Experimental		Theoretical
			% masa	count	count
D	ASP	133,11	2,04	3,24	3
E	GLU + GLN	147,13	3,92	15,35	16
N	ASN	132,12	0,00	0,00	
S	SER	105,09	0,00	0,00	
Q		146,15	0,00	0,00	
H	HIS	151,9	0,80	5,39	6
G	GLY	75,07	28,21	253,28	252
T	THR	119,12	0,74	1,25	1
R	ARG	174,2	1,31	2,11	2
A	ALA	89,1	2,11	6,17	7
Y	TYR	181,19	1,23	3,63	3
C	CYS	240	0,00	0,00	
V	VAL	117,15	26,41	152,72	157
M	MET	149,21	0,39		
W	TRP	204,33	0,75	3,53	4
F	PHE	165,19	0,93	3,84	3
I	ILE	131,18	11,24	65,12	63
L	LEU	131,18	2,71	10,23	9
K	LYS	146,65	0,63	2,97	3
P	PRO	115,13	16,59	110,47	111
			100,00	639,3	640

**B**

**Figure S4.** Characterization of Akt-in polymer. A: The amino acid composition was verified by high performance liquid chromatography (HPLC). B: The molecular weight of the recombinamer was determined by mass spectrometry (MALDI-TOF/MS). MALDI-TOF spectrum represents non-quantitative intensity (a.u.) against  $m/z$  (mass divided by net charge of the molecule) of the ELR. Either the mono charged either the doubly charged recombinamers were detected. The theoretical molecular weight was 55330 Da.

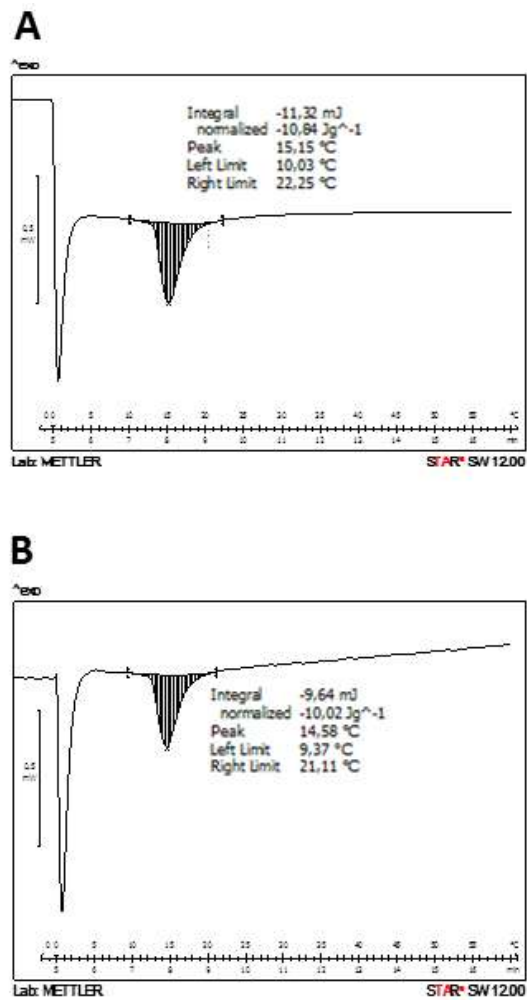


**Figure S5.** Characterization of ELR polymers. Determination of transition temperature ( $T_t$ ) by differential scanning calorimetry (DSC) in PBS (pH 7.4). A: Control polymer. B: Akt-in polymer.

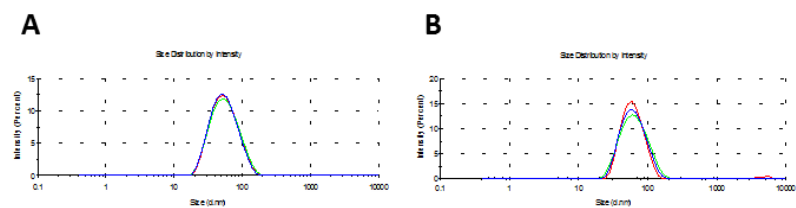


**Figure S6.** Characterization of ELR nanoparticles. Determination of size by dynamic light scattering in PBS buffer (pH 7.4) at 37°C at 0.5 mg/mL. A: Control polymer. B: Akt-in polymer.

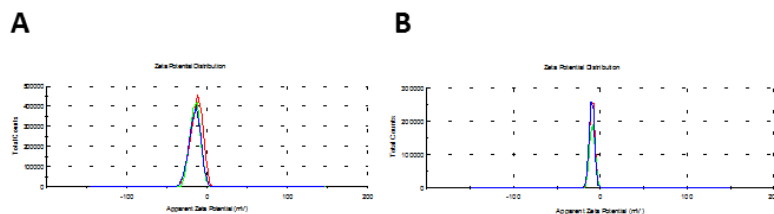


**Figure S7.** Characterization of ELR nanoparticles. Determination of z-potential measured by dynamic light scattering in ultrapure water type I at 37°C at 1 mg/mL. A: Control polymer. B: Akt-in polymer.

Nanoparticle	Time (h)	Size (nm)	PdI	Zeta Potential (mV)
Control NP	0	65.60 ± 3.73	0.087	-27.8 ± 1.5
	1	65.85 ± 3.23	0.070	-26.6 ± 1.4
	2	67.01 ± 2.78	0.134	-28 ± 1.8
	3	66.78 ± 2.46	0.127	-26.6 ± 1.2
Akt-in NP	0	72.46 ± 3.52	0.079	-26.2 ± 1.2
	1	73.2 ± 2.88	0.141	-25.8 ± 1.4
	2	72.08 ± 3.02	0.116	-25.4 ± 1.9
	3	71.71 ± 3.38	0.102	-25.9 ± 1.6

**Table S2.** Characterization of ELR nanoparticles. Size and polydispersity index of self-assembled polymers incubated with 5% BSA at 37°C measured by dynamic light scattering (DLS). Surface charge of self-assembled polymers measured by dynamic light scattering (DLS). Mean ± SD.

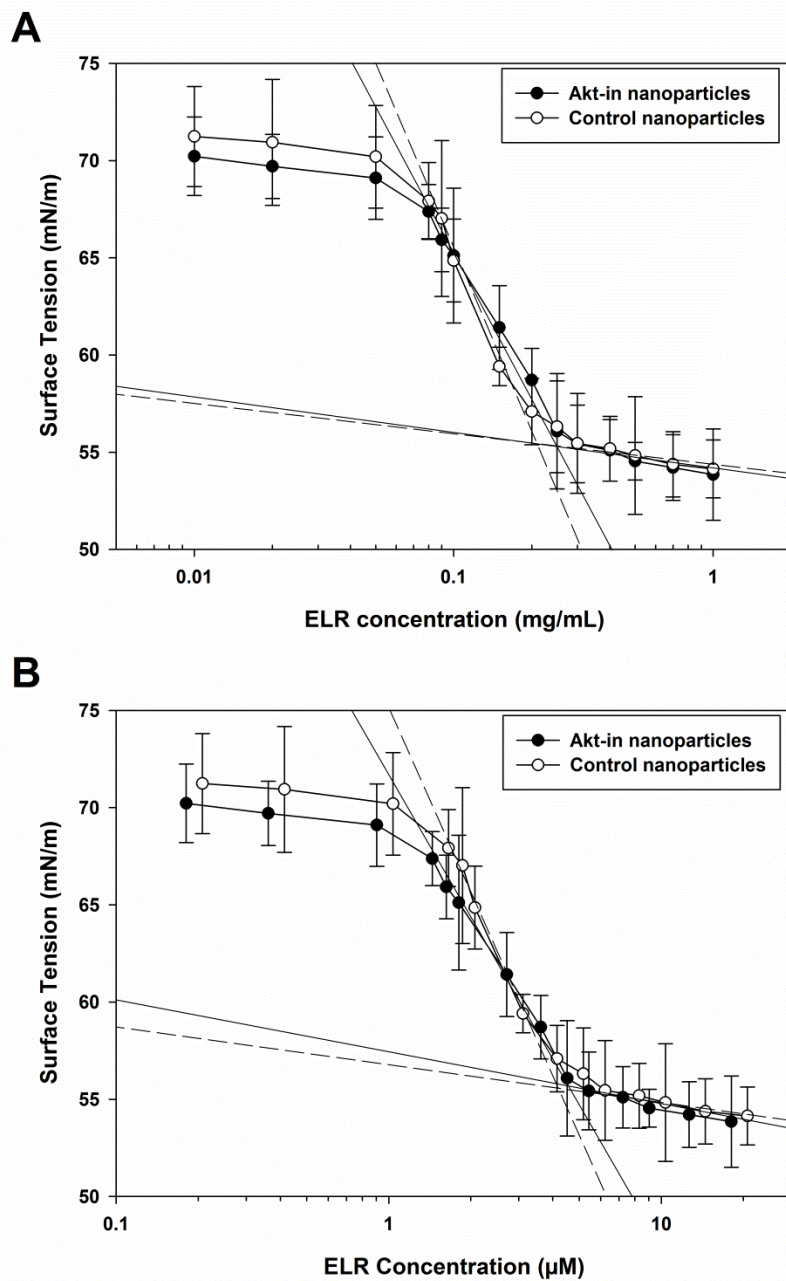


**Figure S8.** Characterization of ELR nanoparticles. Determination of critical micellar concentration (CMC) using the pendant drop method in PBS buffer (pH 7.4).

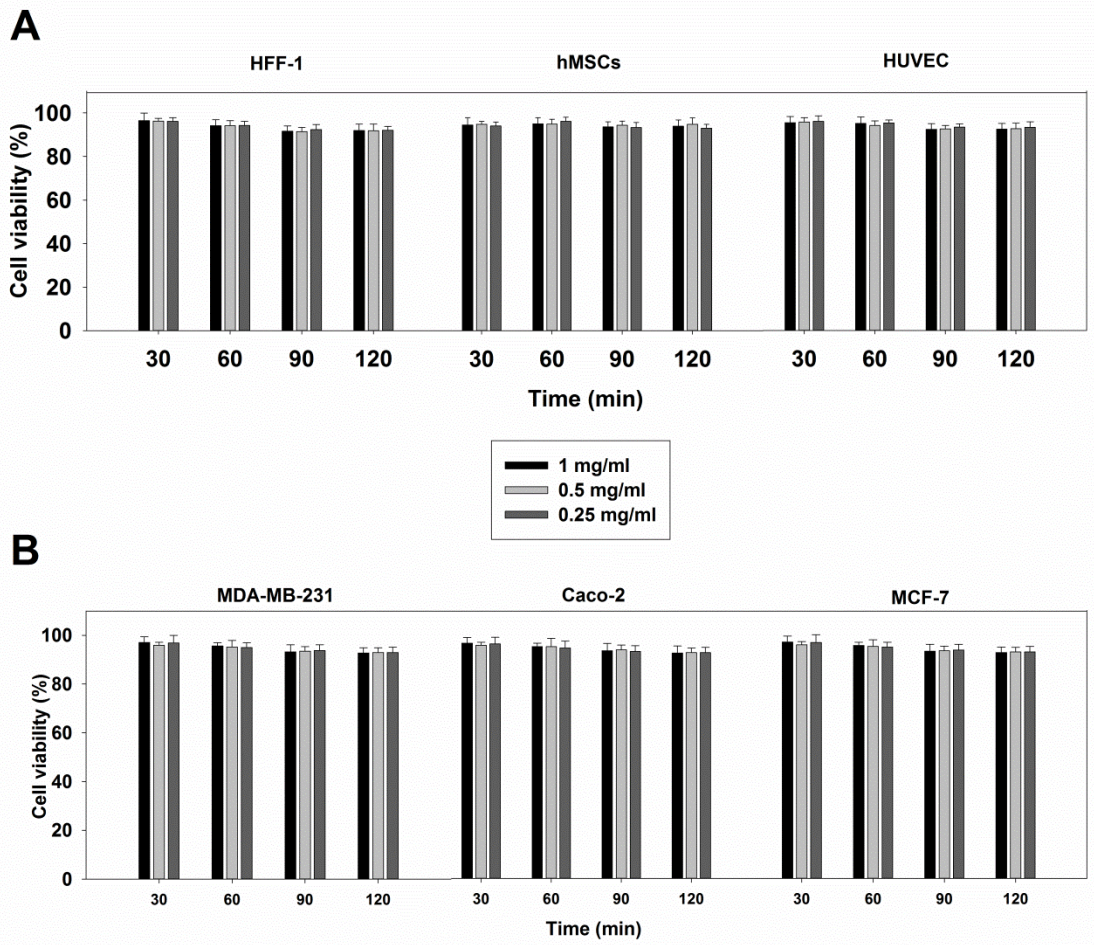


**Figure S9.** Percentage viability for HFF-1, hMSCs and HUVEC (panel A) and MDA-MB-231, Caco-2 and MCF-7 (panel B) with respect to untreated cells. Cells were incubated with control nanoparticles at three concentrations and times and viability was measured using the LIVE/DEAD kit Assay. n = 3 independent experiments, mean ± SD.

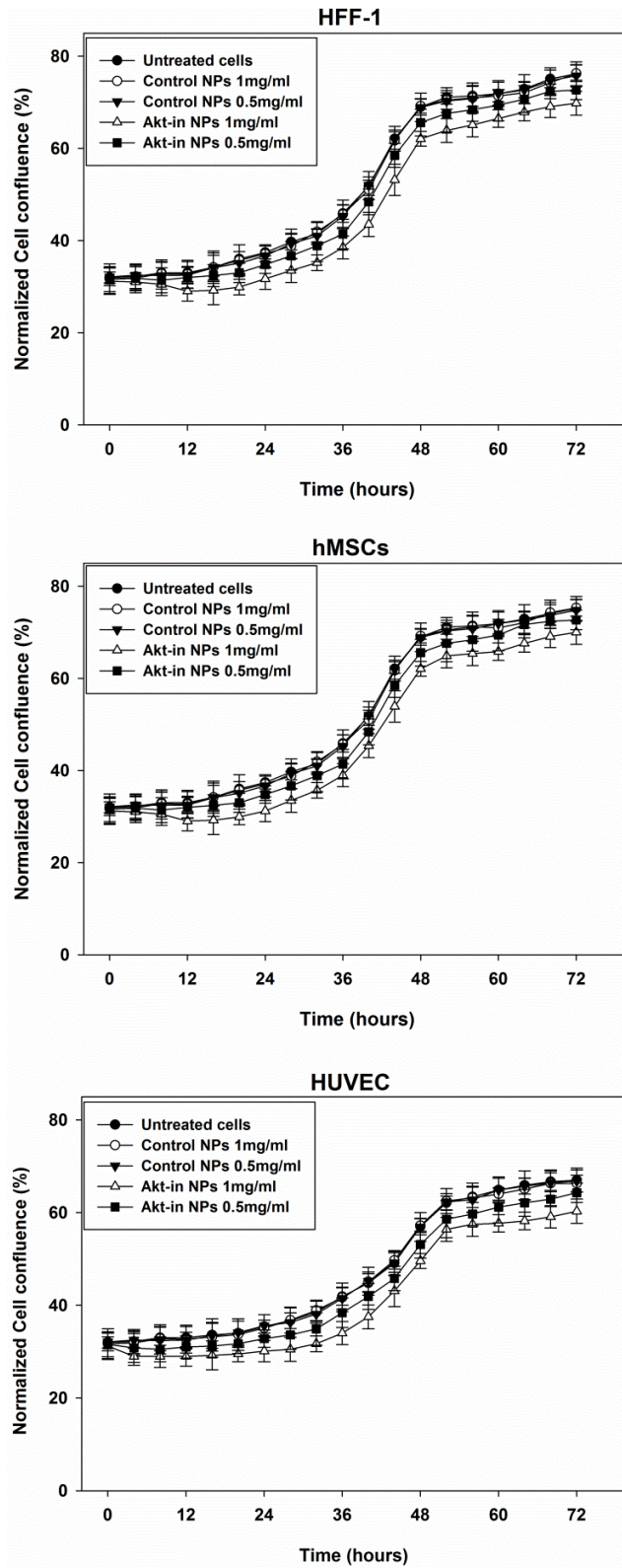


**Figure S10.** Cellular proliferation of non-cancerous cell lines HFF-1 (Top panel), hMSCs (Middle panel) and HUVEC (Bottom panel). Cells were incubated with ELR-based nanoparticles at two different concentrations (1mg/mL and 0.5 mg/mL) for 72 hours. n = 2 independent experiments, mean  $\pm$  SD.